Journal of Power Sources 555 (2023) 232367

Contents lists available at ScienceDirect

Journal of Power Sources

journal homepage: www.elsevier.com/locate/jpowsour

Surface film formation on Mg electrode containing magnesium polysulfides in TFSI-based electrolytes

M. Victoria Bracamonte [a,b,1], Alen Vizintin [c,1], Gregor Kapun [c], Fernando Cometto [d], Jan Bitenc [c], Anna Randon-Vitanova [e], Miran Gaberščček [c,f], Robert Dominko [c,f,g,*]

[a] Instituto Enrique Gaviola (IFEG), CCT Córdoba-CONICET, 5000, Córdoba, Argentina
[b] Facultad de Matemática, Astronomía y Física, Universidad Nacional de Córdoba (UNC), Av. Medina Allende s/n, Ciudad Universitaria, 5000, Córdoba, Argentina
[c] National Institute of Chemistry, Hajdrihova 19, SI-1000, Ljubljana, Slovenia
[d] Departamento de Fisicoquímica, Instituto de Investigaciones en Fisicoquímica de Cordoba, INFIQC-CONICET, Facultad de Ciencias Químicas, Universidad Nacional de Córdoba, Ciudad Universitaria, X5000HUA, Córdoba, Argentina
[e] Honda R&D Europe GmbH, Carl-Legien Strasse 30, 63703, Offenbach, Germany
[f] University of Ljubljana, Faculty of Chemistry and Chemical Technology, Večna pot 113, SI-1001, Ljubljana, Slovenia
[g] ALISTORE - European Research Institute, 33 rue Saint-Leu, Amiens, 80039 Cedex, France

HIGHLIGHTS

- Magnesium passivation in the presence of polysulfides is less resistive.
- A more pronounced pitting corrosion mechanism explains the lower resistance.
- Polysulfides and chlorides in electrolyte create an aggressive environment.
- Thinner passivation layer is formed in the presence of polysulfides.
- Polarization is influenced by transport properties in the electrolyte.

ABSTRACT

A rechargeable magnesium sulfur battery is an attractive redox couple due to the natural abundance of electrode active components and the possibility to offer a suitable energy density at a low price. The sulfur conversion mechanism in the magnesium battery is well known, however, several issues such as the large overpotential, fast capacity fading, and slow reaction kinetics are still under debate and should be properly addressed. At least partially, these problems are related to the passivation of the magnesium surface, due to the interaction with electrolyte/catholyte. Here, we explore the Mg^{2+} deposition/dissolution process on the Mg metal electrode in the presence of $Mg(TFSI)_2/MgCl_2$ in TEGDME:DOL and $MgS_8/Mg(TFSI)_2/MgCl_2$ in TEGDME:DOL electrolytes. We show that an interfacial layer in the presence of polysulfides is less resistive, due to the joint corrosion nature of chlorides and sulfides. This has been confirmed in a combined study using conventional electrochemical experimental techniques supported by modeling of EIS spectra, X-ray photoelectron spectroscopy (XPS), and focused ion beam-scanning electron microscopy (FIB-SEM).

1. Introduction

Li-ion batteries have facilitated a wide adoption of portable electronics, due to their high gravimetric and volumetric energy densities, and acceptable price performance. Additionally, Li-ion batteries are currently the most appropriate existing battery technology in electric mobility. However, contemporary Li-ion batteries utilize several critical raw materials (Co, Ni, Cu, graphite, Li), opening questions of sustainability, geopolitical problems, and large-scale production feasibility [1–3].

For this reason, the batteries' research has been advancing to the frontiers of new systems (Li–S, Li-air, Mg–S, and other combinations of multivalent batteries, etc.), moving beyond the state-of-the-art rocking chair chemistry in terms of energy density, cost, and sustainability [4].

Sulfur is a low-cost and abundant element in the Earth's crust and is therefore an ideal cathode material to couple with the eighth-most earth-abundant element, magnesium. When both elements are paired into an electrochemical couple, it can be expected that the volumetric

* Corresponding author. National Institute of Chemistry, Hajdrihova 19, SI-1000, Ljubljana, Slovenia.
E-mail address: robert.dominko@ki.si (R. Dominko).
[1] These authors contributed equally to this work.

https://doi.org/10.1016/j.jpowsour.2022.232367
Received 8 September 2022; Received in revised form 25 October 2022; Accepted 4 November 2022
Available online 19 November 2022

and gravimetric energy densities will exceed those of contemporary Li-ion batteries [5]. Magnesium-sulfur (Mg–S) battery was firstly demonstrated by Muldoon and co-workers in 2011 [6]. The operation mechanism of the Mg–S battery is based on a conversion reaction of sulfur through polysulfides to MgS and reverse during charge with the source of magnesium coming from the Mg metal anode through the plating/stripping process. Therefore the conversion reactions are similar to those found in Li–S batteries [7–12]. Typically, the discharge of an Mg–S battery in ether-based electrolyte proceeds via two defined plateaus, corresponding to the solid-liquid equilibria between sulfur and long chain polysulfides (high voltage plateau) and between short chain polysulfides and MgS (low voltage plateau) as a final product of discharge [8,13]. However, different salts and solvents can change the reaction pathway by merging the two plateaus, due to different polysulfides solubility constants. The most appropriate solvents for Mg–S batteries are different ethers with high polysulfides solubility. However, at the same time, ether-based electrolytes influence various degradation phenomena such as self-discharge, low cycle life, polysulfide shuttling, and high polarization due to salt precipitation [10,14–16].

New non-nucleophilic electrolyte concepts with weakly coordinating magnesium salts have been developed to overcome the short cycle lifetime and facilitate ion-pair dissociation [7,10,17–19]. However, there are still open questions about processes at the surface/interphase of the Mg anode. Typically, the Mg metal electrode is covered with a solid surface film, impeding the transport of magnesium ions. Therefore, a component that facilitates the Mg plating/stripping process is added [20,21]. That does not prevent degradation reactions close to the electrode surface and consequently the formation of a passivation layer. The decomposition products, together with other species that are present in the electrolyte can lead to a formation of either a beneficial solid-electrolyte-interphase (SEI) or a blocking passivation film [22,23]. For that reason, it is important to analyze the composition of the resulting passivation film and to understand the reactions leading to the formation of the passive layer. With the presence of additional components in the electrolyte, such as dissolved polysulfides, the reaction mechanism, and degradation products can be even more complicated.

Herein, we focus on a study of an Mg electrode interface in an Mg $(TFSI)_2$, $MgCl_2$ ether-based electrolyte with and without the presence of polysulfides. The (electro)chemically formed surface films were carefully analyzed by employing electrochemical methods (galvanostatic/potentiostatic, electrochemical impedance spectroscopy (EIS), and cyclic voltammetry), focused ion beam-scanning electron microscopy (FIB-SEM) and X-ray photoelectron spectroscopy (XPS). By combining different characterization techniques, we show the impact of polysulfides in the electrolyte on the corrosion mechanism and related morphological/chemical changes within the passivation layer formed on the magnesium metal surface.

2. Experimental part

2.1. Materials

All the materials, electrolytes, and cell assembly were kept and prepared inside an Ar-filled glovebox (MBraun; $O_2 < 1.0$ ppm, $H_2O < 1.0$ ppm). The $Mg(TFSI)_2$ salt (Solvionic, 99.5%) was dried at 225 °C for 3 days under vacuum, $MgCl_2$ salt (ultradry, Alfa Aesar, 99.99% metal trace) was used as received, solvents (tetraethylene glycol dimethyl ether (TEGDME), 1,3-dioxolane (DOL)) were dried in a multistep process using molecular sieves, and distillation, after which the water content was measured by Karl Fischer titration (Mettler Toledo, C20) and kept below 2 ppm. Magnesium polysulfide was synthesized as Mg $[N\text{-MeIm}]_6S_8$ complex according to the literature [16,24].

2.2. Electrochemistry

Two electrodes symmetrical Mg||Mg pouch-type cells were assembled with 2 cm^2 polished Mg disks (Mg metal foil from Changsha Rich Nonferrous metals 0.1 mm thickness, purity 99.95%). 40 μL of different electrolytes: a) 0.4 M $Mg(TFSI)_2$, 0.4 M $MgCl_2$ in TEGDME:DOL (1:1 vol%), b) 10 mM MgS_8 in 0.4 M $Mg(TFSI)_2$, 0.4 M $MgCl_2$ in TEGDME:DOL and c) 0.8 M $Mg(TFSI)_2$ in TEGDME:DOL, were used to soak the glass fiber separator (Whatman GF/A). All electrochemical experiments were performed using a BioLogic VMP3 potentiostat/galvanostat. Potentiostatic electrochemical impedance spectroscopy (PEIS) measurements were performed at 25 °C in the frequency range from 1 MHz to 10 mHz with an amplitude of 14.1 mV. Impedance spectra were calculated according to the procedure given in supplementary data. The calculations and plotting were carried out in Python 3.8 using our code. An example of the code for EIS simulation together with the specific impedance output is given in the supplementary data. Cyclic voltammetry (CV) measurements on symmetrical Mg||Mg cells were run in the range from 0.8 V and −0.8 V vs. the potential of the counter electrode (Mg/Mg^{2+}) with a sweep rate of 0.1 mV s^{-1}. Stripping and deposition tests were performed using 0.1 mA cm^{-2} current density for 2 h. Cells were kept at OCV for different periods (0 min, 30 min, and 24 h) before being connected to the potentiostat/galvanostat.

2.3. Microscopy

Focused Ion Beam – Scanning electron Microscope (FIB-SEM) Helios Nanolab 650i (FEI, USA) was used to analyze the *post-mortem* Mg electrodes. The cells were opened inside an Ar-filled glovebox and washed with THF and DME to remove the excess of salts. The samples were placed on a custom-made holder, which was closed inside the glovebox and transferred throughout the C1010 airlock loading system (Gatan, US) into the FIB-SEM vacuum chamber. Electrode surface imaging was obtained at 2 kV (50 pA) using a standard ETD detector. Detailed surface film and morphology images were acquired at 1 kV (13 pA) using beam deceleration mode (200 V stage biasing) and an in-column integrated TLD detector. Before cross-sectional analysis, the surface was protected with 1 μm of Pt layer by inducing Pt-organo-metallic precursor using Ga^+ focused ion beam (FIB) at 30 kV (2.5 nA). Ion beam polished cross-sections were made using FIB at 30 kV (9.4 nA) with the sequential reducing current down to 0.43 nA in a final polishing step. Cross-sectional images were acquired at 2 kV (50 pA) using a TLD detector. Phase contrast images were recorded at 2 kV (0.4 nA) by detecting low-loss backscattered electrons with a TLD-BSE detector. EDX mapping analysis was performed at low kV analytical conditions (5 kV@ 0.8 nA). Subsequently, each elemental map was post-processed using the TrueQ algorithm (AZtec 3.1, Oxford, UK).

2.4. X-ray photoemission spectroscopy

X-ray photoemission spectroscopy (XPS) measurements were performed with a K-Alpha™ X-ray Photoelectron Spectrometer (using non-monochromatized Al-Kα 1200W). An electron flood gun was used for sample neutralization. An Ar^+ ion beam of 2 keV with a 45-degree incidence was used for sputtering the surface for depth profiling. XPS spectra were recorded for the cycled Mg electrode top surface as well as for the depth profiling sputtered for 30 s, 150 s, and 330 s. The fitting of these spectra was performed using the Avantage® software with a Shirley background using peaks with a 30% Lorentzian, and 70% Gaussian product function. S *2p* spectra were fit with spin−orbit split *2p* 3/2 and *2p* 1/2 doublets, constrained by 1.18 eV separation consistent with the spin−orbit splitting and a characteristic 2:1 area ratio. Cl *2p* spectra were fit with spin−orbit split *2p* 3/2 and *2p* 1/2 doublets, constrained by 1.6 eV separation and a characteristic 2:1 area ratio. The XPS measurements were calibrated from the spurious C *1s* peak at 284.8 eV.

3. Results and discussion

Using the recent progress in understanding the reactivity of

polysulfides in Li–S and Mg–S cells [16,25–27], we here carry out a deeper follow up study in order to clarify several remaining questions. Specifically, we simplify the system to a symmetrical Mg||Mg electrode cell to probe the spurious effects of (i) anode impedance contributions, (ii) unwanted reactions between the polysulfides in solution and Mg anode surface and (iii) the visualization/characterization of the (electro) chemically formed surface films. In Fig. 1 the electrochemical characterization of typical symmetrical Mg||Mg cells is presented. The tests were performed in two electrolytes, a reference one denoted as a TFSI/Cl electrolyte (0.4 M $Mg(TFSI)_2$ 0.4 M $MgCl_2$ in TEGDME:DOL (1:1 vol%)) and an electrolyte containing MgS_8 denoted as a catholyte (0.4 M $Mg(TFSI)_2$ 0.4 M $MgCl_2$, 0.01 M MgS_8 in TEGDME:DOL (1:1 vol%)). Constant amounts of TFSI/Cl electrolyte or catholyte were used for wetting the separator. The electrochemical impedance spectroscopy (EIS) measurements were performed at OCV in the frequency range of 1 MHz ~ 10 mHz prior to any stripping/deposition processes (Fig. 1a). The presented Nyquist plots are raw EIS spectra. Instead of fitting them with arbitrary circuits, we have introduced an impedance model (based on a general interfacial admittance for two adsorbed intermediates), which is described in more detail in the next section. A typical Nyquist plot, obtained from the raw EIS spectra for the cell with a TFSI/Cl electrolyte shows a depressed semicircle, which increases over time. This semicircle can be assigned to the adsorption of species from the electrolyte to the Mg surface creating a passivation layer [28,29]. Such behavior is in good agreement with previous reports, where an adsorption layer formed by electrolyte species on the Mg surface was observed for other magnesium electrolytes [10,21,30]. The formation of the passivation layer is observed as an increase of the resistance due to the charge transfer reaction, which is expressed as an overpotential of 0.25 V for the stripping/deposition process in the symmetrical cell (Fig. 1b). The formed film remains stable as long as no current is applied. Once the galvanostatic test is started, this layer is removed. This is more clearly shown in Fig. 2 where an initial voltage spike exists after 24 h at OCV. This spike indicates the substantial interfacial resistance associated with the adsorption layer. In the absence of $MgCl_2$, and provided that the concentration of magnesium ions is kept the same, e.g. 0.8 M Mg^{2+} (increased content of $Mg(TFSI)_2$ salt), almost an order of magnitude higher overpotential was observed (Fig. S1a). That points out the role of $MgCl_2$ which affects the interface properties on the magnesium surface enabling the stripping and deposition process at lower overpotentials [31]. To further understand the formation of the passive layer, we measured cyclic voltammograms (CV) on a symmetrical two electrode Mg||Mg cell (Fig. 1c). In the anodic scan, the current exhibits a very small peak at around 0.05 V vs. Mg/Mg^{2+} (Fig. S1b), most likely related to oxidizable compound(s) at the surface of the Mg foil or the formation of a thin nanometric film from the Mg^{2+} ion-catalyzed polymerization of 1,3-dioxolane [32]. When the anodic polarization reaches a critical potential (E_{pit}), the current rises suddenly (pitting current), indicating the initiation and growth of a pitting attack [33]. Since E_{pit} is directly related to the quality of the Mg surface, it can vary from cell to cell due to differences in the native passive film and impurities present at the Mg surface. During the cathodic scan, the pitting current exhibits a hysteresis loop, forming a peak with a maximum of around 0.5 V vs. Mg/Mg^{2+} and decreasing rapidly reaching a similar value as before E_{pit}. Also, during the second scan, a cathodic peak occurs at – 0.5 V vs. Mg/Mg^{2+} most likely related to the removal of species formed during the previous scan [34]. Considering these results, two potential regions can be distinguished: i) the region without initiation or propagation of pits ($E < E_{pit}$) and ii) the region where the pits initiate and propagate without any control ($E \geq E_{pit}$). The reproducibility of present results may be estimated from Fig. S1c, which shows three identical symmetrical Mg||Mg cells tested in the TFSI/Cl electrolyte. The stripping and deposition of magnesium in these three cells are not identical, which points towards an uncontrolled pitting from the Mg surface. This behavior can be explained from the CV, where at electrode potentials below the pitting potential, transient transitions related to the formation of metastable pits are observed (Fig. S1d) [33]. Moving towards a higher cycle number, the CVs show an increase in the peak current and a decrease in the peak potential, indicating that the corrosion processes are favored (Fig. S1d). In parallel, the galvanostatic measurement evidence the presence of a new process – observed as steps where the potential increases to absolute values higher than 0.6 V. These processes are even

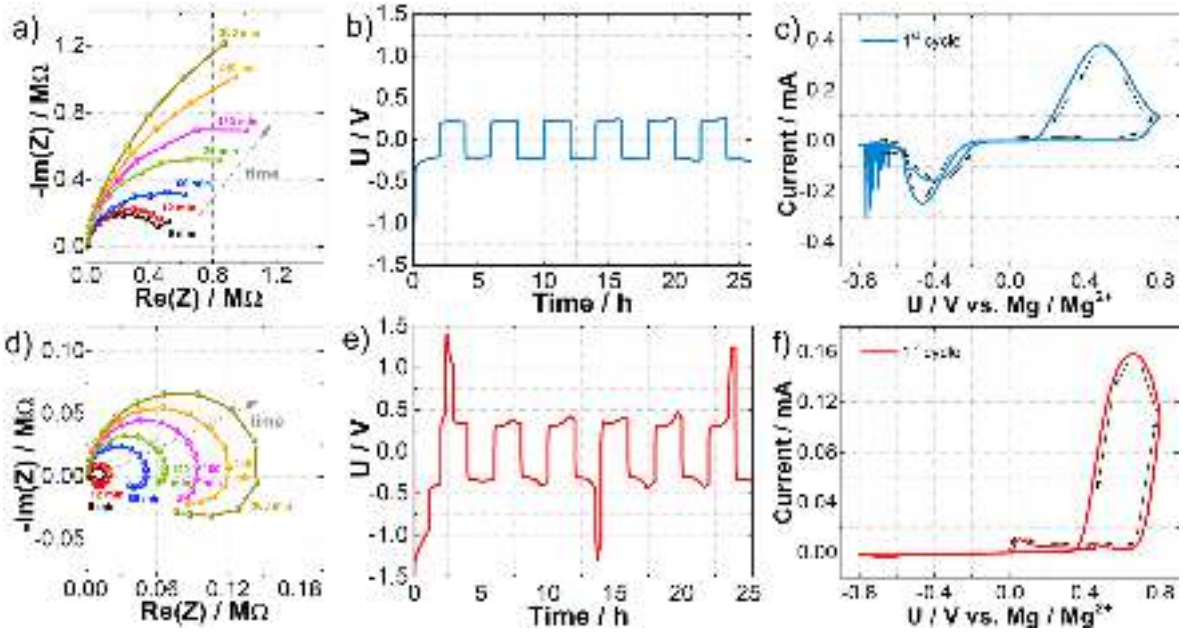

Fig. 1. a-c) Symmetrical Mg||Mg cells in TFSI/Cl electrolyte. **a)** Nyquist plots of symmetrical cells (as a function of time) under OCV. The dashed arrow represents an evolution of spectra with time. **b)** stripping/deposition profiles with a current density of 0.1 mA cm^{-2} and 2 h as a cut-off. **c)** CV with a sweep rate of 0. 1 mV s^{-1} in the voltage range from 0.8 to −0.8 V and **d-f)** Symmetrical Mg||Mg cells in catholyte; **d)** Nyquist plots of symmetrical cells (as a function of time) under OCV. The dashed arrow represents an evolution of spectra with time. **e)** stripping/deposition profiles with a current density of 0.1 mA cm^{-2} and 2 h as cut-off and **f)** CV with a sweep rate of 0. 1 mV s^{-1} in the voltage range from 0.8 to −0.8 V.

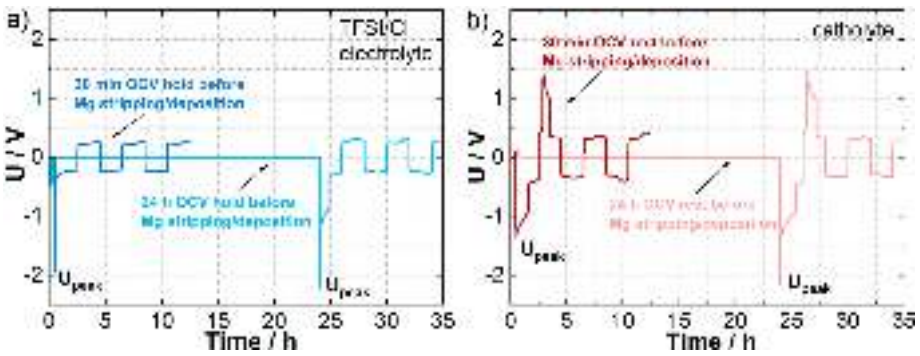

Fig. 2. Symmetrical Mg||Mg cells with 30 min and 24h OCV period and at a current density of 0.1 mA cm^{-2} and 2 h as cut-off with a) TFSI/Cl electrolyte and b) catholyte.

more evident when the potential cut-off was increased to 1.25 V (Figs. S1e–f) and the pit initiates and propagates for longer times. The uncontrolled uneven film breakdown is shown as a current transient for the TFSI/Cl electrolyte (Fig. S1e) and catholyte (Fig. S1f) in the cathodic scan. The current suffers uncontrollable spikes with pit propagation and film breakdown, which stopped the CV measurements. Summarizing these initial results, we can conclude that a spontaneous formation of a passivation layer is observed at the surface of the electrodes in the TFSI/Cl electrolyte. Maintaining the cell at OCV conditions, the impedance grows with time, reaching low-frequency magnitude values higher than 1.2 MΩ after 22 h. However, the film formed at OCV is not fully insulating or compact since the stripping/deposition process occurs at overpotentials of 0.25 V at the current density of 0.1 mA cm^{-2}. This result is in good agreement with the cyclic voltammetry profile, from which a potential range without any corrosion processes is established in the limit of ±0.6 V vs. OCV.

Comparative studies were performed with the catholyte. Fig. 1d shows the evaluation of Nyquist plots measured at OCV conditions with time. Spectra can be divided into two different parts: a) a capacitive loop at high-to-medium frequencies and b) an inductive loop at low frequencies, which is associated with a relaxation process of adsorbed species on the electrode surface [35]. Despite the presence of two corrosive species in the solution i.e. Cl^- and S_8^{2-} anions, we can attribute the stronger effect to MgS_8. Namely, the presence of polysulfides decreases the magnitude of the capacitive arc and invokes the inductive behavior typical for active adsorbates. From these results, we can speculate on the presence of a non-stable layer on the magnesium surface, which is a product of the competition between the adsorption phenomenon (described below) and the corrosion process. The stripping and deposition of magnesium in the presence of catholyte (Fig. 1e) show a higher overpotential (around 0.4 V) and variations in the absolute value of overvoltage from the first cycle. The cyclic voltammogram of symmetrical Mg||Mg cell with catholyte is shown in Fig. 1f. During the anodic scan, three electrochemical processes can be distinguished: a) the peak at 0.25 V vs. Mg/Mg^{2+} which can be attributed to the Mg^{2+} ion-catalyzed polymerization of 1,3-dioxolane, and the attack of a nucleophilic (S_x^{2-} species) [32,36], b) an unassigned sharp peak at 0.45 V vs. Mg/Mg^{2+} and c) the pitting attack at a potential higher than 0.65 V vs. Mg/Mg^{2+}. It is important to notice that the second anodic peak is not constant, and its position is not comparable between different experiments [33]. During a cathodic scan, only a small peak of corrosion product is observed at −0.6 V vs. Mg/Mg^{2+}. The definition of a stable potential range in the presence of polysulfides is not possible, since the pitting attack is not the only process affecting the electrochemical performance of the symmetrical Mg||Mg cells.

A deeper analysis of the film formation in the symmetrical Mg||Mg cells with TFSI/Cl electrolyte and catholyte at OCV was performed studying the evaluation of polarization with time (U_{peak}). Cells had been left at OCV for conditioning for different periods (0 min, 30 min, and 24h) before stripping and deposition tests were applied (Fig. 2). As shown in Table 1, the initial polarization in the TFSI/Cl electrolyte exhibits a value of ~2.04 V for the period of measurements. By contrast, in the presence of polysulfides (Fig. 2b) the U_{peak} measured after 30 min of rest at OCV appears at a lower overpotential. These results are in good agreement with the EIS results (Fig. 1a,d), showing a less resistive film formed on the Mg surface in the presence of polysulfides as a product of the competition between the TFSI reaction and the S_8^{2-} pitting attack. With a prolonged resting period, the U_{peak} increases, indicating that TFSI adsorption is the predominant reaction during a prolonged resting period.

To explain the difference in the electrochemical behavior of cells containing the TFSI/Cl electrolyte and the catholyte, we briefly introduce a general impedance model (see supplementary data and Fig. S2) that explains the trends observed in Fig. 1a and d. In the absence of polysulfides, the interaction of magnesium with electrolyte is assumed to generally be via a two-step corrosion reaction. This reaction mechanism proceeds through two consecutive one-electron transfer reactions with an adsorbed intermediate denoted as Mg_{ads}^+:

$$Mg \underset{k_2}{\overset{k_1}{\rightleftarrows}} Mg_{ads}^+ + e^- \quad (1)$$

$$Mg_{ads}^+ \underset{k_4}{\overset{k_3}{\rightleftarrows}} Mg^{2+} + e^- \quad (2)$$

where k_i is a potential dependent rate constant, $k_i = k_{0,i}\exp\left(\frac{z\alpha_i F}{RT}\right) = k_{0,i}\exp(b_i E)$. Here $k_{0,i}$ is the rate at $E = 0$ determined with respect to a selected reference potential, z is the number of electrons exchanged in the step, α_i is the transfer coefficient, F is the Faraday's constant, R is the gas constant and T is temperature. Calculating the total current due to Eqs. (1) and (2), taking account of the system's mass balance and transforming it into frequency space, one readily gets the so-called faradaic impedance due to reactions (1) and (2) (see supplementary data on general interfacial admittance for two adsorbed intermediates). Adding the impedance of the double-layer capacitance one gets the total impedance of the interface. Any mass transport impedance is here neglected as the interfacial impedance appears to have very high values.

Table 1
Values of the initial potential drop of symmetrical Mg||Mg cells in TFSI/Cl electrolyte and catholyte.

Conditioning time	U_{peak}/V	
	TFSI/Cl electrolyte	Catholyte
Fresh	−2.04 ± 0.40 V	−1.5 ± 0.1 V
30 min	−1.94 ± 0.04 V	−1.37 ± 0.01 V
24 h	−2.22 ± 0.02 V	−2.15 ± 0.04 V

In the case when in addition to the main corrosion reaction there are other important interfacial contributions, one needs to extend the mechanism of Eqs. (1) and (2). In the present case we assume the following general scheme (extension by two steps):

$$Mg^{+}_{ads} + A^{-} \underset{K_6}{\overset{K_5}{\rightleftarrows}} MgA_{ads} \quad (3)$$

$$MgA_{ads} \underset{k_8}{\overset{k_7}{\rightleftarrows}} Mg^{2+} + e^{-} + A^{-} \quad (4)$$

where A^{-} is a general species in the electrolyte that can catalyze the main corrosion reaction. As noted above, such a species can be chloride anions, Cl^{-} but also S_x^{2-} species. As evident from the experimental results, we here assume that the main catalytic effect in the present electrolyte composition comes from the polysulfide anions while the effect of chlorides is neglected. Namely, we can see that the presence of polysulfides decreases the average impedance values by about an order of magnitude concerning the situation where only chlorides are present. Thus, in the first approximation one may neglect the eventual kinetics of chlorides even if there may be a small contribution of adsorbed chlorides to the total impedance as well. Note that in contrast to the other 3 reactions, Eq. (3) involves no charge transfer, i.e. it is considered a chemical reaction. The faradaic impedance for the mechanism that involves all 4 reactions can be calculated analogously as mentioned above for the 2-reaction mechanism (see supplementary data on general interfacial admittance for two adsorbed intermediates).

Fig. 3 shows calculated impedance spectra reproducing the trends observed in Fig. 1a and d. As mentioned above, for the case without polysulfides, only equations (1) and (2) were considered while in the case of the presence of polysulfides we considered all 4 equations (Eqs. (1)–(4)).

Examples of parameter values for a typical simulated spectrum in the presence and absence of polysulfides are shown in Table S1. A more detailed study of these values and their trends reveals that one cannot get trends of shapes displayed in Fig. 3b without assuming at least two different adsorbed species, for instance, Mg^{+}_{ads} and MgA_{ads}. In other words, trends observed in Fig. 1a and d cannot be reproduced with more a simple mechanism, in particular the size and magnitude of the apparent inductive loop at low frequencies. By contrast, as seen from a comparison of Figs. 3a and 1a, in the case of the absence of polysulfides the trends are much simpler (no inductive loop) and a simple mechanism (Eq. (1) and (2)) suffices to reproduce these trends. As a whole, one may conclude that these simulations support the assumption that polysulfides serve as catalysts, i.e. they enhance the (electro)chemical interaction of magnesium with electrolyte. In both cases, however, the main reason for increasing the impedance value is the decrease of the value of k_3 (see Eq. (2)). In the physical sense, this means that the transfer of adsorbed species on the magnesium surface becomes progressively more difficult with time. One might interpret this as a tendency for the surface species to remain on the surface rather than dissolve into the electrolyte. This observation is also in the agreement with U_{peak} values presented in Table 1.

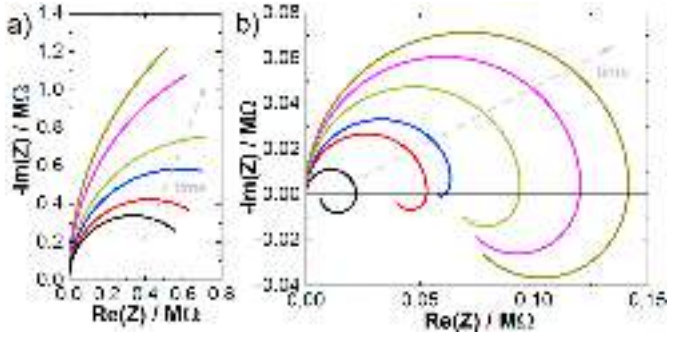

Fig. 3. Simulated impedance spectra that mimic the behavior of measurements presented in Fig. 1a (left) and 1d (right). All the spectra on the left are based on Eqs. (1) and (2) whereas the spectra on the right include all 4 reactions (Eqs. (1)–(4)).

Further visualization of the formed passive layer at the surface was performed by *post-mortem* FIB-SEM on the fresh and cycled symmetrical Mg||Mg cells in TFSI/Cl electrolyte and catholyte (Fig. 4). The formed passive layer was further confirmed by the ATR-IR spectroscopy (more information can be found in the supplementary data and in Figs. S3–S4). A fresh Mg electrode has a rough surface, which is due to mechanical surface polishing (Fig. 4a). After a prolonged Mg stripping and deposition, the surface is unevenly covered by degradation products (Fig. 4b) and with spherical agglomerates with a diameter of 8 μm. This is in good agreement with a previous literature report [37] and explains the scattered electrochemical results of the three cells shown in Fig. S1c. The visualized surface morphology points toward an uneven film growth and therefore uncontrolled pitting from the Mg surface. Similar surface morphology was found at the surface of Mg electrodes cycled in the catholyte (Fig. 4c) and in a more concentrated TFSI electrolyte (Fig. S5).

EDX mapping of the magnesium electrode surface after cycling (Fig. S6a) confirms the presence of degradation products (Mg, F, O, Cl, and S) from the TFSI/Cl electrolyte. Quantitative EDX spectra from selected different area positions revealed similar chemical compositions of the surface film (Fig. S6b). This points out that the surface film is formed from different species, such as MgO, MgF_2, MgS, $MgCl_2$, sulfates, and organic products. In contrast, a quantitative analysis of EDX spectra at point 2, where the macroscopic film was not visibly present, showed the presence of 91.2 ± 0.5 wt% Mg, 4.7 ± 0.3 wt% O, 3.1 ± 0.4 wt% C and 1.0 ± 0.3 wt% F (Fig. S6b). This is most likely due to a peel-off during the separation of the separator and electrode. Based on these results we can say that the uneven film growth on the Mg electrode surface – in a form of thick film or spherical particles – is due to an uneven TFSI surface decomposition.

Fig. 4d shows a FIB-polished cross-section of the fresh Mg electrode. A polycrystalline morphology of Mg is well observed. The bulk of the cycled Mg electrodes is not changed concerning non-cycled magnesium (Fig. 4d–f). The interphase of the Mg electrode with TFSI/Cl electrolyte is pitted and covered with a porous film with a thickness of around 10 μm (Fig. 4e). Fig. S7 shows the mapping and quantitative EDX of the FIB-polished cross-section. Similar to the surface, the porous film is composed of all elements and species detected at the surface, with the elements being homogeneously distributed. The porous nature of the passivation layer based on the TFSI/Cl electrolyte degradation products is most likely the main reason for its random breakage which in turn results in uncontrolled electrochemical processes, as observed in Fig. 1. The passive film formed on the Mg electrode during cycling in a catholyte (Fig. 4f) is thinner with more easily detected pits. This is in good agreement with the EIS results (Fig. 1d) which suggested a more aggressive corrosion environment in the presence of polysulfides along chlorides. The EDX mapping and quantitative EDX spectra (Figs. S8–S9) show similar element distribution compared to TFSI/Cl electrolyte.

To further elaborate on the chemical composition of the formed films, X-ray photoelectron spectroscopy (XPS) analysis was performed on Mg electrodes cycled in TFSI/Cl electrolyte, catholyte, and concentrated TFSI electrolyte as a reference. To gain information beyond the outermost surface layer, we performed a set of XPS measurements after exposing the electrodes to Ar^{+} ion sputtering during 30 s, 60 s, 150 s, and 330 s sputter times. The evolution of the elemental composition (in the percentage of Mg, O, F, C, Cl, and S atoms after relative sensitivity factors corrections) of the electrodes before and after sputtering, are depicted in Tables 2 and 3 and Table S2. In addition, Fig. 5 and Figs. S10–S12 show the specific XPS analysis of the different species found after sputtering in the S *2p*, Mg *2p*, O *1s*, F *1s,* and Cl *2p* regions.

In both, the TFSI/Cl electrolyte and the catholyte, the concentration

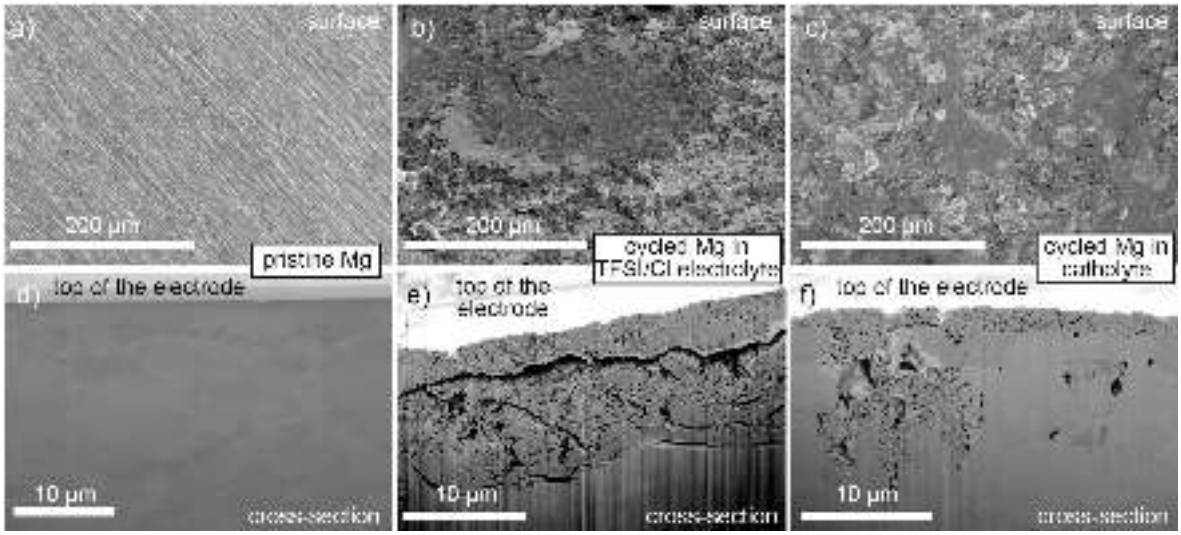

Fig. 4. Top-down view of magnesium electrodes: a) pristine, b) cycled magnesium electrode in TFSI/Cl electrolyte, c) cycled magnesium electrode in catholyte; and corresponding FIB-polished cross-sections: d) pristine, e) cycled magnesium electrode in TFSI/Cl electrolyte and f) cycled magnesium electrode in catholyte.

Table 2
Atomic elemental composition for Mg electrode in TFSI/Cl electrolyte.

Ar^+ ion sputter time/s	C at. %	O at. %	Mg at. %	F at. %	S at. %	Cl at. %
0	23.3	39.7	21.6	10.8	1.9	2.8
30	6.4	37.1	40.4	9.9	1.5	4.8
60	5.9	36.8	42.8	10.4	1.1	3.1
150	4.4	37.5	44.4	10.9	0.1	2.7
330	2.8	38.4	44.56	11.7	0.1	2.5

Table 3
Atomic elemental composition for Mg electrode in catholyte.

Ar^+ ion sputter time/s	C at. %	O at. %	Mg at. %	F at. %	S at. %	Cl at. %
0	48.5	28.1	9.0	7.9	2.7	3.9
30	12.5	32.2	37.5	14.3	2.2	2.9
60	12	31.2	36.0	13.1	2.5	2.8
150	11.5	30.1	38.6	13.7	2.4	3.1
330	9.3	28.9	40.9	14.9	2.6	3.3

of elemental Mg increases with the sputtering time which is mainly due to the presence of $MgCl_2$, MgO, MgF_2, and MgS (Figs. S10–S12). In contrast, using a concentrated TFSI electrolyte, we observed a more pronounced increment in elemental Mg, due to the presence of metallic Mg. To better understand the obtained results, the Mg *2p* XPS spectra of a polished foil (dashed lines in Figs. S10–S12) as a blank Mg is included. The separation between the metallic and the oxidized features at the metallic foil is about 1.7 eV. In all the cycled Mg electrodes, the separation is higher (2.0–3.0 eV) and the peak becomes broader. This confirms the presence of other Mg species rather than only MgO. Note that the deconvolution of Mg *2p* spectra for quantification purposes could be problematic, due to the proximity of the binding energies of the different species and the impossibility to fit them by separated terms. Therefore, the quantification of Mg compounds (other than metallic Mg) is performed by the analysis of S *2p*, F *1s*, O *1s,* and Cl *2p* spectra (Fig. 5 and Figs. S10–S12). The F concentration increases with sputtering time for both investigated electrolytes (TFSI/Cl electrolyte and catholyte) (Tables 2 and 3). In the F *1s* spectra (Figs. S10–S11), two well-defined peaks are observed - before sputtering - at around 685.5 eV and 688.5 eV which can be attributed to both, C–F_x species (from TFSI) [38] and MgF_2 [39,40], respectively. Notice that the main peak in both samples belongs to MgF_2 and was attributed to TFSI decomposition – which is the only possible source of F in the cell. After sputtering, only MgF_2 as fluorine-containing species is observed in the sample, demonstrating its presence in the formed interphase layer. Comparatively, in samples cycled in concentrated TFSI the dominant peak, before sputtering, is the one related to C–F_x that belongs to non-decomposed adsorbed TFSI species (Fig. S10). While after sputtering, it is still present in a higher amount compared to TFSI/Cl electrolyte and catholyte, indicating the trapping of non-decomposed TFSI in the inner part of the formed surface film. The same trend is observed from S *2p* spectra before sputtering (Fig. 5), where the different peaks attributed to MgS (161.3–161.6 eV) [11,39] and S–S (S_x) (163.1–164.0 eV) [7,11] are found on Mg electrode in TFSI/Cl electrolyte and catholyte, while in concentrated TFSI electrolyte (Fig. S10) the main peak belongs to O═S═O species (at 169.1 eV) [38] from intact TFSI (absence of neither sulfides nor polysulfides). From these results, we can conclude that in all cases, the topmost part of the interphase layer contains electrolyte species, which can be absorbed in the surface and only small amounts of decomposed electrolyte salts, while the composition of the inner part is dependent on the used salts. All the binding energies – obtained by the fitting procedure of each S *2p* spectrum – attributed to different S compounds are summarized in Table S3. Further analysis of the S composition is presented in Tables S4–S6 where the total percentage of S elemental compositions (corrected by relative sensitivity factors) and the discrimination of the different S compounds compositions obtained by the fitting of each S *2p* XPS spectrum are shown. It can be noticed that, in the sample cycled in TFSI/Cl electrolyte, the S composition decreases with the Ar^+ ion exposure time, from 2.0 at.% to 0.1 at.% after 330 s, and the presence of reduced S compounds can be detected in the inner layers. A different scenario is found for the sample cycled in catholyte; the total amount of S compounds remains almost constant in the inner layers, 2.6 at.% on average. This is due to the increase of the MgS amount in the inner layers and the consequent vanishing of oxidized S compounds. To summarize, the differences observed by XPS at the interphases formed in different electrolytes complement and support the results obtained with FIB-SEM where different morphologies were observed, and electrochemistry, where the reactivity was dependent on the used electrolyte.

4. Conclusion

The structure and properties of the interphase film covering the Mg metal anode depend on the type of electrolyte. More pronounced changes are observed with additives enabling activation/corrosion of

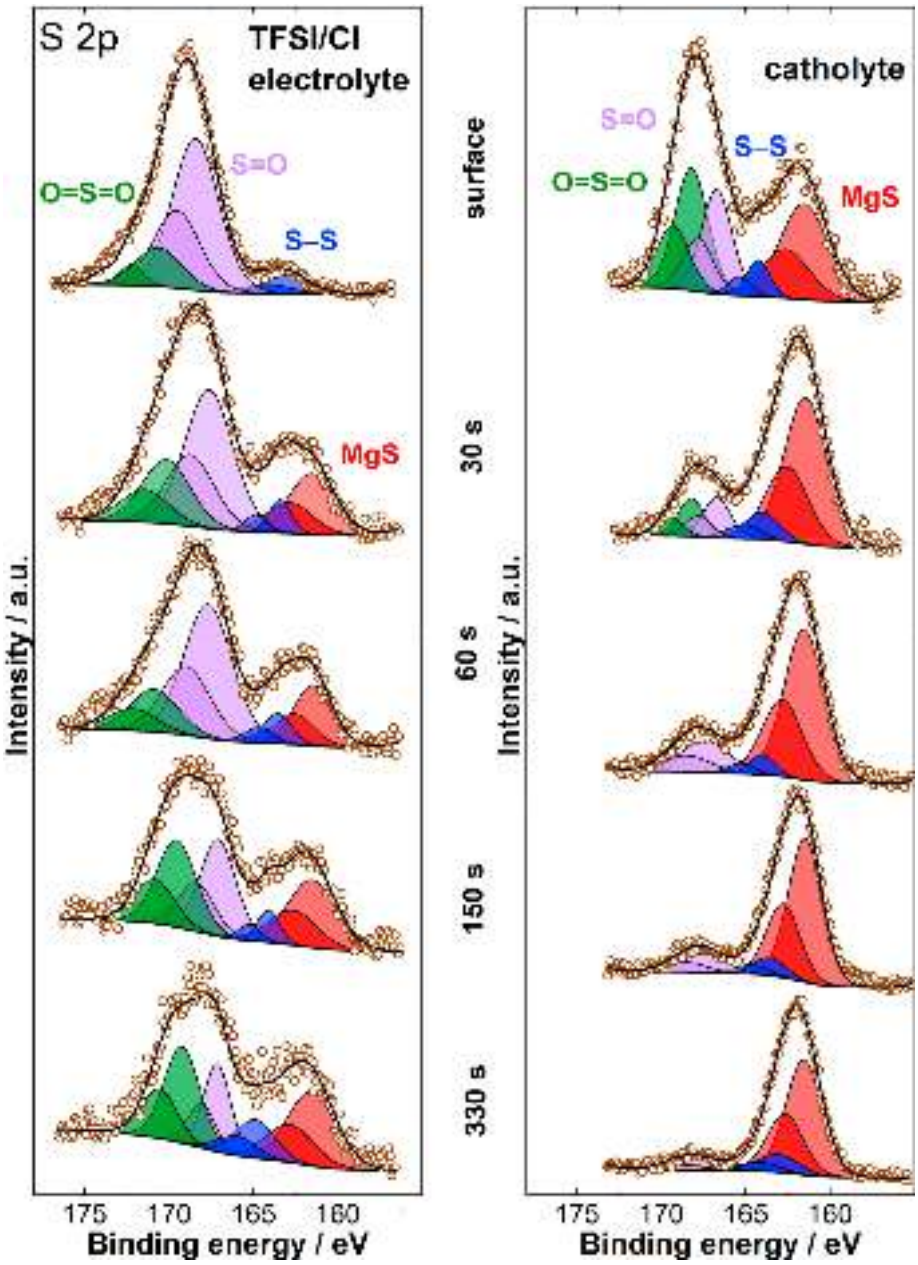

Fig. 5. S 2p spectra of pristine and after 30 s, 60 s, 150 s, and 330 s of Ar^+ ion sputtering for Mg electrodes in **a)** TFSI/Cl electrolyte and **b)** catholyte.

the magnesium surface. We show that polysulfides - together with chlorides - in the electrolyte form a more aggressive corrosion environment which influences the structural and chemical properties of the passivation layer on Mg metal. EIS and voltammetry reveal the formation of an interphase layer, which grows with time and suffers from significant corrosive attacks that are more pronounced in the presence of polysulfides. Consequently, the overpotential needed to break a passive film formed at OCV conditions at the Mg electrode interface in the electrolyte without polysulfides is higher (around 2.0 V) compared with the selected catholyte (1.5 V). This can be related to the formation of a more homogenous passive layer, due to the absence of polysulfides. However, the initial lower resistance in cells containing the electrolyte with polysulfides is not demonstrated as a lower polarization for the stripping and deposition process. That was explained by a FIB-SEM study, which revealed the presence of a 10 μm thick porous passive film on the top of the magnesium electrode after cycling in TFSI/Cl electrolyte. By contrast, in the case of catholyte a thinner (around 3 μm) porous passive film was observed on the electrode surface. Another major difference between the two electrolytes is the presence of a larger number of pits when polysulfides are present in the electrolyte. A more pronounced pitting corrosion mechanism, which is visible by FIB-SEM, explains the lower polarization needed for breaking the passive film and lower resistance, as suggested by the evolution of measured EIS spectra. However, the higher polarization observed in the stripping and deposition test is influenced by transport properties.

EDX studies showed that the film on the cycled Mg electrode is composed of Mg, F, O, Cl, C, and S elements which are homogeneously distributed across the electrode. XPS measurements revealed that the chemical composition of the passive film depends on the electrolyte and changes across the film depth. In all studied electrolytes the topmost layer is formed mainly from MgS, MgF, and MgO originating from the decomposed electrolyte. Analyzing the sulfur species, a non-reacted TFSI is found in deeper layers and the concentrated TFSI electrolyte only. MgS and oxidized species were detected in TFSI/Cl whereas mainly MgS was found in the catholyte.

The present findings reveal how the presence of Cl^- and S_8^{2-} can

strongly determine the composition of the solid electrolyte interphase which consequently has a pronounced influence on the cell's electrochemical performance during the Mg^{2+} stripping/deposition processes. Although polysulfides are deposited on the surface, they do not completely block/passivate the Mg electrode.

CRediT authorship contribution statement

M. Victoria Bracamonte: Conceptualization, Methodology, Formal analysis, Investigation, Writing – original draft. **Alen Vizintin:** Conceptualization, Methodology, Formal analysis, Investigation, & data analysis, Writing – original draft, Visualization. **Gregor Kapun:** Investigation, & data analysis, Writing – review & editing. **Fernando Cometto:** Investigation, & data analysis, Writing – review & editing. **Jan Bitenc:** Investigation, Writing – review & editing. **Anna Randon-Vitanova:** Writing – review & editing. **Miran Gaberšček:** Formal analysis, Writing – review & editing. **Robert Dominko:** Conceptualization, Supervision, Writing – review & editing, Project administration, Funding acquisition.

Declaration of competing interest

The authors declare the following financial interests/personal relationships which may be considered as potential competing interests: Robert Dominko reports financial support was provided by Honda R&D Europe GmbH. Robert Dominko reports equipment, drugs, or supplies was provided by CENN Nano center Slovenia.

Data availability

Data will be made available on request.

Acknowledgment

This research was supported by the Slovenian Research Agency (research projects Z2-1863, N2-0266, and research core funding P2-0423 and P2-0393) and by Honda R&D Europe (Germany). CENN Nanocenter Slovenia is also acknowledged for using the FIB-SEM instrument Helios NanoLab 650.

Appendix A. Supplementary data

Supplementary data to this article can be found online at https://doi.org/10.1016/j.jpowsour.2022.232367.

References

[1] M. Armand, J.M. Tarascon, Building better batteries, Nature 451 (2008) 652–657, https://doi.org/10.1038/451652a.
[2] V. Etacheri, R. Marom, R. Elazari, G. Salitra, D. Aurbach, Challenges in the development of advanced Li-ion batteries: a review, Energy Environ. Sci. 4 (2011) 3243, https://doi.org/10.1039/c1ee01598b.
[3] J.M. Tarascon, M. Armand, Issues and challenges facing rechargeable lithium batteries, Nature 414 (2001) 359–367, https://doi.org/10.1038/35104644.
[4] D. Larcher, J.-M. Tarascon, Towards greener and more sustainable batteries for electrical energy storage, Nat. Chem. 7 (2015) 19–29, https://doi.org/10.1038/nchem.2085.
[5] R. Dominko, J. Bitenc, R. Berthelot, M. Gauthier, G. Pagot, V. Di Noto, Magnesium batteries: current picture and missing pieces of the puzzle, J. Power Sources 478 (2020), 229027, https://doi.org/10.1016/j.jpowsour.2020.229027.
[6] H.S. Kim, T.S. Arthur, G.D. Allred, J. Zajicek, J.G. Newman, A.E. Rodnyansky, A. G. Oliver, W.C. Boggess, J. Muldoon, Structure and compatibility of a magnesium electrolyte with a sulphur cathode, Nat. Commun. 2 (2011) 427, https://doi.org/10.1038/ncomms1435.
[7] Z. Zhao-Karger, X. Zhao, D. Wang, T. Diemant, R.J. Behm, M. Fichtner, Performance improvement of magnesium sulfur batteries with modified non-nucleophilic electrolytes, Adv. Energy Mater. 5 (2015), 1401155, https://doi.org/10.1002/aenm.201401155.
[8] A. Robba, A. Vizintin, J. Bitenc, G. Mali, I. Arčon, M. Kavčič, M. Žitnik, K. Bučar, G. Aquilanti, C. Martineau-Corcos, A. Randon-Vitanova, R. Dominko, Mechanistic study of magnesium-sulfur batteries, Chem. Mater. 29 (2017), https://doi.org/10.1021/acs.chemmater.7b03956.
[9] X. Yu, A. Manthiram, Performance enhancement and mechanistic studies of magnesium-sulfur cells with an advanced cathode structure, ACS Energy Lett. 1 (2016) 431–437, https://doi.org/10.1021/acsenergylett.6b00213.
[10] Z. Zhao-Karger, R. Liu, W. Dai, Z. Li, T. Diemant, B.P. Vinayan, C. Bonatto Minella, X. Yu, A. Manthiram, R.J. Behm, M. Ruben, M. Fichtner, Toward highly reversible magnesium–sulfur batteries with efficient and practical $Mg[B(hfip)_4]_2$ electrolyte, ACS Energy Lett. 3 (2018) 2005–2013, https://doi.org/10.1021/acsenergylett.8b01061.
[11] T. Gao, S. Hou, F. Wang, Z. Ma, X. Li, K. Xu, C. Wang, Reversible S 0/MgS x redox chemistry in a $MgTFSI_2/MgCl_2$/DME electrolyte for rechargeable Mg/S batteries, Angew. Chem. Int. Ed. 56 (2017) 13526–13530, https://doi.org/10.1002/anie.201708241.
[12] P. Wang, M.R. Buchmeiser, Rechargeable magnesium–sulfur battery technology: state of the art and key challenges, Adv. Funct. Mater. 29 (2019), 1905248, https://doi.org/10.1002/adfm.201905248.
[13] R. Dominko, A. Vizintin, G. Aquilanti, L. Stievano, M.J. Helen, A.R. Munnangi, M. Fichtner, I. Arcon, Polysulfides formation in different electrolytes from the perspective of X-ray absorption spectroscopy, J. Electrochem. Soc. 165 (2018) A5014–A5019, https://doi.org/10.1149/2.0151801jes.
[14] S. Drvarič Talian, G. Kapun, J. Moškon, A. Vizintin, A. Randon-Vitanova, R. Dominko, M. Gaberšček, Which process limits the operation of a Li-S system? Chem. Mater. (2019) https://doi.org/10.1021/acs.chemmater.9b03255.
[15] S. Chung, A. Manthiram, Current status and future prospects of metal–sulfur batteries, Adv. Mater. 31 (2019), 1901125, https://doi.org/10.1002/adma.201901125.
[16] S. Drvarič Talian, A. Vizintin, J. Bitenc, G. Aquilanti, A. Randon-Vitanova, M. Gaberšček, R. Dominko, Magnesium polysulfides: synthesis, disproportionation, and impedance response in symmetrical carbon electrode cells, Chemelectrochem 8 (2021) 1062–1069, https://doi.org/10.1002/celc.202100041.
[17] Z. Zhao-Karger, M.E. Gil Bardaji, O. Fuhr, M. Fichtner, A new class of non-corrosive, highly efficient electrolytes for rechargeable magnesium batteries, J. Mater. Chem. A. 5 (2017) 10815–10820, https://doi.org/10.1039/C7TA02237A.
[18] T. Gao, X. Ji, S. Hou, X. Fan, X. Li, C. Yang, F. Han, F. Wang, J. Jiang, K. Xu, C. Wang, Thermodynamics and kinetics of sulfur cathode during discharge in $MgTFSI_2$-DME electrolyte, Adv. Mater. 30 (2018), 1704313, https://doi.org/10.1002/adma.201704313.
[19] T. Pavčnik, M. Lozinšek, K. Pirnat, A. Vizintin, T. Mandai, D. Aurbach, R. Dominko, J. Bitenc, On the practical applications of the magnesium fluorinated alkoxyaluminate electrolyte in Mg battery cells, ACS Appl. Mater. Interfaces 14 (2022) 26766–26774, https://doi.org/10.1021/acsami.2c05141.
[20] D. Aurbach, H. Gizbar, A. Schechter, O. Chusid, H.E. Gottlieb, Y. Gofer, I. Goldberg, Electrolyte solutions for rechargeable magnesium batteries based on organomagnesium chloroaluminate complexes, J. Electrochem. Soc. 149 (2002) A115, https://doi.org/10.1149/1.1429925.
[21] O. Tutusaus, R. Mohtadi, N. Singh, T.S. Arthur, F. Mizuno, Study of electrochemical phenomena observed at the Mg metal/electrolyte interface, ACS Energy Lett. 2 (2017) 224–229, https://doi.org/10.1021/acsenergylett.6b00549.
[22] A. Kopač Lautar, J. Bitenc, T. Rejec, R. Dominko, J.-S. Filhol, M.-L. Doublet, Electrolyte reactivity in the double layer in Mg batteries: an interface potential-dependent DFT study, J. Am. Chem. Soc. 142 (2020) 5146–5153, https://doi.org/10.1021/jacs.9b12474.
[23] M. Salama, R. Attias, B. Hirsch, R. Yemini, Y. Gofer, M. Noked, D. Aurbach, On the feasibility of practical Mg-S batteries: practical limitations associated with metallic magnesium anodes, ACS Appl. Mater. Interfaces (2018) 8b11123, https://doi.org/10.1021/acsami.8b11123, acsami.
[24] G. Bieker, J. Wellmann, M. Kolek, K. Jalkanen, M. Winter, P. Bieker, Influence of cations in lithium and magnesium polysulphide solutions: dependence of the solvent chemistry, Phys. Chem. Chem. Phys. 19 (2017) 11152–11162, https://doi.org/10.1039/c7cp01238a.
[25] S. Drvarič Talian, J. Moškon, R. Dominko, M. Gaberšček, Reactivity and diffusivity of Li polysulfides: a fundamental study using impedance spectroscopy, ACS Appl. Mater. Interfaces 9 (2017) 29760–29770, https://doi.org/10.1021/acsami.7b08317.
[26] S. Drvarič Talian, A. Vizintin, J. Moškon, R. Dominko, M. Gaberšček, Electrochemical kinetics study of interaction between Li metal and polysulfides, J. Electrochem. Soc. 167 (2020), 080526, https://doi.org/10.1149/1945-7111/ab8ed1.
[27] S. Drvarič Talian, J. Bobnar, J. Moškon, R. Dominko, M. Gaberšček, Effect of high concentration of polysulfides on Li stripping and deposition, Electrochim. Acta 354 (2020), 136696, https://doi.org/10.1016/j.electacta.2020.136696.
[28] D. Aurbach, Magnesium deposition and dissolution processes in ethereal Grignard salt solutions using simultaneous EQCM-EIS and in situ FTIR spectroscopy, Electrochem. Solid State Lett. 3 (1999) 31, https://doi.org/10.1149/1.1390949.
[29] D. Aurbach, Y. Gofer, A. Schechter, O. Chusid, H. Gizbar, Y. Cohen, M. Moshkovich, R. Turgeman, A comparison between the electrochemical behavior of reversible magnesium and lithium electrodes, J. Power Sources 97–98 (2001) 269–273, https://doi.org/10.1016/S0378-7753(01)00622-X.
[30] J. Häcker, C. Danner, B. Sievert, I. Biswas, Z. Zhao-Karger, N. Wagner, K. A. Friedrich, Investigation of magnesium–sulfur batteries using electrochemical impedance spectroscopy, Electrochim. Acta 338 (2020), 135787, https://doi.org/10.1016/j.electacta.2020.135787.
[31] M. Salama, I. Shterenberg, L.J.W. Shimon, K. Keinan-Adamsky, M. Afri, Y. Gofer, D. Aurbach, Structural analysis of magnesium chloride complexes in dimethoxyethane solutions in the context of Mg batteries research, J. Phys. Chem. C 121 (2017) 24909–24918, https://doi.org/10.1021/acs.jpcc.7b05452.

[32] E. Sahadeo, Y. Wang, C.-F. Lin, Y. Li, G. Rubloff, S.B. Lee, Mg^{2+} ion-catalyzed polymerization of 1,3-dioxolane in battery electrolytes, Chem. Commun. 56 (2020) 4583–4586, https://doi.org/10.1039/D0CC01769H.
[33] E. McCafferty, Crevice corrosion and pitting, in: Introd. To Corros. Sci., Springer, New York, NY, 2010, pp. 263–313, https://doi.org/10.1007/978-1-4419-0455-3_10.
[34] S.S. Mahapatra, J. Datta, Characterization of Pt-Pd/C electrocatalyst for methanol oxidation in alkaline medium, Int. J. Electrochem. 2011 (2011) 1–16, https://doi.org/10.4061/2011/563495.
[35] R. Attias, B. Dlugatch, M.S. Chae, Y. Goffer, D. Aurbach, Changes in the interfacial charge-transfer resistance of Mg metal electrodes, measured by dynamic electrochemical impedance spectroscopy, Electrochem. Commun. 124 (2021), 106952, https://doi.org/10.1016/j.elecom.2021.106952.
[36] L. Lodovico, A. Varzi, S. Passerini, Radical decomposition of ether-based electrolytes for Li-S batteries, J. Electrochem. Soc. 164 (2017) A1812–A1819, https://doi.org/10.1149/2.0311709jes.
[37] M.S. Ding, T. Diemant, R.J. Behm, S. Passerini, G.A. Giffin, Dendrite growth in Mg metal cells containing Mg(TFSI) 2/Glyme electrolytes, J. Electrochem. Soc. 165 (2018) A1983, https://doi.org/10.1149/2.1471809jes. –A1990.
[38] R. Dedryvère, S. Leroy, H. Martinez, F. Blanchard, D. Lemordant, D. Gonbeau, XPS valence characterization of lithium salts as a tool to study electrode/electrolyte interfaces of Li-ion batteries, J. Phys. Chem. B 110 (2006) 12986–12992, https://doi.org/10.1021/jp061624f.
[39] T. Gao, S. Hou, K. Huynh, F. Wang, N. Eidson, X. Fan, F. Han, C. Luo, M. Mao, X. Li, C. Wang, Existence of solid electrolyte interphase in Mg batteries: Mg/S chemistry as an example, ACS Appl. Mater. Interfaces 10 (2018) 14767–14776, https://doi.org/10.1021/acsami.8b02425.
[40] S. Mertin, L. Marot, C.S. Sandu, R. Steiner, J.-L. Scartezzini, P. Muralt, Nanocrystalline low-refractive magnesium fluoride films deposited by reactive magnetron sputtering: optical and structural properties, Adv. Eng. Mater. 17 (2015) 1652–1659, https://doi.org/10.1002/adem.201500129.